Figuring Out Gas & Galaxies in Enzo (FOGGIE). II. Emission from the z=3 Circumgalactic Medium

Draft version June 22, 2020
Typeset using LaTeX **twocolumn** style in AASTeX62

Figuring Out Gas & Galaxies in Enzo (FOGGIE). II. Emission from the $z = 3$ Circumgalactic Medium

Lauren Corlies,[1,2] Molly S. Peeples,[3,1] Jason Tumlinson,[3,1] Brian W. O'Shea,[4] Nicolas Lehner,[5] J. Christopher Howk,[5] John M. O'Meara,[6,7] and Britton D. Smith[8]

[1] *Department of Physics & Astronomy, Johns Hopkins University, 3400 N. Charles Street, Baltimore, MD 21218*
[2] *Rubin Observatory Project Office, 950 N. Cherry Ave., Tucson, AZ 85719*
[3] *Space Telescope Science Institute, 3700 San Martin Drive, Baltimore, MD, 21218*
[4] *Department of Computational Mathematics, Science and Engineering, Department of Physics and Astronomy, National Superconducting Cyclotron Laboratory, Michigan State University, East Lansing, MI 48823*
[5] *Department of Physics, University of Notre Dame, Notre Dame, IN 46556*
[6] *Department of Physics, St. Michael's College, Colchester, VT 05439*
[7] *W. M. Keck Observatory, Waimea, HI 96743*
[8] *Institute for Astronomy, University of Edinburgh, Royal Observatory, Edinburgh EH9 3HJ, UK*

ABSTRACT

Observing the circumgalactic medium (CGM) in emission provides 3D maps of the spatial and kinematic extent of the gas that fuels galaxies and receives their feedback. We present mock emission-line maps of highly resolved CGM gas from the FOGGIE project (Figuring Out Gas & Galaxies in Enzo) and link these maps back to physical and spatial properties of the gas. In particular, we examine the ionization source leading to most O VI emission and how resolution affects the physical properties of the gas generating the emission. Finally, when increasing the spatial resolution alone, the total luminosity of the line emission increases by an order of magnitude for some lines considered. Current IFU instruments like KCWI and MUSE should be able to detect the brightest knots and filaments of such emission, and use this to infer the bulk kinematics of the CGM gas with respect to the galaxy. We conclude that the spatial resolution of simulated CGM gas can significantly influence the distribution of gas temperatures, densities, and metallicities that contribute to a given observable region. Greater spatial resolution than has been typically included in cosmological simulations to date is needed to properly interpret observations in terms of the underlying gas structure driving emission.

Keywords: galaxies: evolution — galaxies: circumgalactic medium — hydrodynamics

1. INTRODUCTION

Diffuse gas that is within galactic halos but outside the star-forming disk, referred to as the circumgalactic medium (CGM), is critical to how galaxies evolve (Tumlinson, Peeples, & Werk 2017). This gas is comprised of metal-poor inflows from the intergalactic medium (IGM), metal-rich outflows from supernova (SN), feedback in the galactic disk, and intermediate metallicity gas that is mixed as gas recycles onto the disk or is stripped from in-falling satellite galaxies. While these processes are all readily seen in simulations, observing them in emission remains difficult because the high temperatures and low densities of the gas shift most of the emission to ultraviolet wavelengths and low surface brightnesses. Using the FOGGIE (Figuring Out Gas & Galaxies In Enzo) simulations, we show here that changing the resolution of the CGM alone can change the distribution of the physical properties of the gas and affects predictions and interpretations of observable circumgalactic emission.

At low redshift, CGM absorption measurements have been connected to galaxy properties (Stocke et al. 2013; Tumlinson et al. 2013; Werk et al. 2014; Bordoloi et al. 2014; Liang & Chen 2014; Borthakur et al. 2016; Keeney et al. 2018; Berg et al. 2018). However, such samples are inherently limited by the number of UV bright quasars needed to make the absorption measurements. At high redshift ($z \gtrsim 2$), the lines probing this gas have shifted into visible wavelengths. Studies of damped Lyman-α

Corresponding author: Lauren Corlies
lcorlies@lsst.org

absorbers (DLAs; Wolfe et al. 2005; Neeleman et al. 2013; Rafelski et al. 2016), super Lyman limit systems / sub-DLAs (Péroux et al. 2008; Som et al. 2015; Fumagalli et al. 2016; Quiret et al. 2016), Lyman limit systems (LLSs; Lehner et al. 2014; Fumagalli et al. 2016; Lehner et al. 2016), and partial LLSs (Lehner et al. 2016) have long shown large amounts of dense H I and corresponding metals throughout the universe. Yet the redshift that puts these absorption lines within reach also shifts key line diagnostics of the associated galaxies into the infrared and out of the range of easy detection by current instrumentation. Thus, relating the absorption features to their galactic environment at high-z has remained challenging (though see Rudie et al. 2012, 2013; Turner et al. 2014, 2015, 2017).

In contrast, observing the CGM directly in *emission* promises to help us understand the spatial and kinematic distribution of the gas around a single galaxy. Yet emission studies have faced similar challenges when trying to resolve their sources. Metal-line emission observations remain limited, with some evidence for extended O VI emission at low-z (Hayes et al. 2016). Instead, emission from the relatively bright Lyα line thus far provides the most insight into the spatial extent of the CGM in emission observations. Recently, two powerful new integral field units (IFUs) on 8–10m class telescopes—the Multi Unit Spectroscopic Explorer (MUSE) on the VLT (Bacon et al. 2010) and the Keck Cosmic Web Imager (KCWI) on Keck (Morrissey et al. 2018)—have provided exciting new tools with which to detect spatially extended Lyman-α emission. Looking to quasars as triggers for bright emission from the gas surrounding them, most at $2 < z < 3$, have measurable Lyα profiles extending as far as 80 kpc from the galaxy on average (Arrigoni Battaia et al. 2018a), while a handful have detected emission as distant as 200–300 kpc (Borisova et al. 2016; Arrigoni Battaia et al. 2018b; Cai et al. 2018). For galaxies, MUSE has revealed Lyα around nearly every galaxy it has observed in the high-z universe (Wisotzki et al. 2016, 2018) though generally for a smaller median extent of 4–5 kpc (Leclercq et al. 2017). Though the source of this ionization is still unclear (Prescott et al. 2015), IFUs probe the dynamics of the gas (Martin et al. 2014; Swinbank et al. 2015) in an effort to help understand the source and fate of the CGM.

Because of their high velocities, outflows have been easier to identify and more ubiquitous than their inflowing counterparts, which remain mostly elusive. Down-the-barrel observations of nearby (Zheng et al. 2017) and more distant galaxies (Rubin et al. 2012) provide the only limited extragalactic evidence for inflows. The Milky Way itself provides the most detailed understanding of large complexes of H I and surveys of high-velocity clouds that shape the inflow of gas onto our own galactic disk (see Putman et al. 2012, for a review).

The new wave of instrumentation and observations means that the CGM has placed unique and powerful constraints on galaxy formation simulations in recent years. Most simulations, independent of code, have had difficulties reproducing both the H I and O VI distributions at low-z (see Tumlinson et al. 2017, for a review). Most approaches for rectifying this difference have invoked various forms of feedback such as: stronger supernova feedback (Hummels et al. 2013; Ford et al. 2016), active galactic nuclei (AGN) feedback (Suresh et al. 2017; Oppenheimer et al. 2018), cosmic ray feedback (Salem et al. 2016; Butsky & Quinn 2018), and non-equilibrium ionization effects (Oppenheimer et al. 2016), among others. Instead of changing the sub-grid physics routines, this work looks at the foundation of the simulation itself - the resolution scheme - to understand how implicit, numerical choices can affect the unresolved CGM.

Additionally, these simulations all employ absorption data as their constraints. Fewer simulations have provided predictions for emission measurements to compare to observations. The most obvious choice of prediction would be the distribution of Lyα emission. However, while Lyα can tell us much about the CGM, there are advantages to searching for the dimmer emission driven by metal lines. First, because Lyα is a resonant line, untangling the structure of the emitting gas versus the gas scattering Lyα photons is challenging and requires modeling of the radiative transfer (Lake et al. 2015; Dijkstra & Kramer 2012; Zheng et al. 2011). Moreover, Lyα necessarily traces the relatively cool, dense gas preferred by H I. Metal lines, on the other hand, can probe the full range of densities, temperatures, and ionization states expected in the CGM because of the large number of available transitions. Metal lines also trace the gas flows that drive galaxy evolution and set the physical properties of the CGM itself.

Because metal-line emission is expected to be extremely faint, simulations have the potential to help guide the search for detectable targets. Typically, these studies have looked at cosmological samples of galaxies to better understand the entire population since resolving smaller physical scales was challenging. Bertone & Schaye (2012) established which lines emit the most brightly in the CGM and highlighted the strong dependency of the emission on both the gas density and temperature in relation to the cooling curves of the emitting ions. Sravan et al. (2016) explored the variable

nature of CGM emission and discussed how detectable emission will be biased towards galaxies having recently experienced large starburst events. In their work at low-z, Bertone et al. (2010) also demonstrated the relative insensitivity of emission to changes in the simulation's feedback prescriptions because of its strong bias to high densities. Frank et al. (2012) highlighted the strength of CGM emission relative to IGM emission, indicating that it was a good candidate for direct detection. Corlies & Schiminovich (2016) focused on low-z emission around a single galaxy and found that the brightest emission follows the filament structure of the halo, and determined that simulation resolution indeed limits the ability to draw physical conclusions. However, while these studies mention the relevance of the predictions for upcoming instrumentation, only Frank et al. (2012) makes specific instrument-focused predictions for FIREBall (Tuttle et al. 2008) from their simulations and Augustin et al. (2019) for FIREBall-2 and HARMONI.

In this paper, we analyze the first generation of the FOGGIE simulations, wherein we take a novel approach where the spatial resolution in the CGM of a Milky Way-like galaxy is forced to be as high as the resolution in the galactic disk, an improvement of 8–32× better than what is typically found in similar simulations (though see recent work from van de Voort et al. 2019, Suresh et al. 2018, Rhodin et al. 2019, and Hummels et al. 2018). Previous theoretical work has made efforts to extend high resolution into the CGM but with explicit focus on dense, cold accretion (Rosdahl & Blaizot 2012) or with higher resolution still concentrated on tracing the mass (Mitchell et al. 2018). Our approach simulating the *entire* circumgalactic volume at the enhanced resolution is agnostic to gas properties.

With this new approach to resolving the CGM, we investigate how our predictions of emission from this gas change due to **changing *only* the resolution at which the gas is simulated**. In particular, we investigate how the observable properties of the gas change owing to the physical properties of the gas. While our focus is on $z = 3$ to maximize the number of lines observable by current ground-based IFUs while minimizing the effects of surface brightness dimming, these lessons are broadly applicable to $2 \lesssim z \lesssim 4$ when the galaxy has passed the first stages of star formation but has not finished merging into the final, massive galaxy.

In Section 2, we present the simulations and the refinement method that allows us to achieve such high resolution in the outer halo. In Section 3, we make predictions for CGM metal-line emission and examine how the results change with resolution. In Section 4, we link the changes in observable properties to changes in the physical, ionization state of the gas. In Section 5, we make specific predictions for different observing modes of KCWI and MUSE for easy comparison with future observations. Finally, in Section 6 we discuss the broader context of our results and summarize our conclusions in Section 7.

2. SIMULATIONS AND METHODS

The cosmological hydrodynamic simulations we analyze here are the same as presented in Peeples et al. (2019, hereafter Paper I); the full details of the simulations and our novel "forced refinement" scheme are given there. We briefly review the highlights in Section 2.1; in Section 2.2, we describe how we calculate emissivities from these simulations.

2.1. *Simulation Basics*

The FOGGIE simulations were evolved with with Enzo, an Eulerian adaptive mesh refinement (AMR) grid-based hydrodynamic code (Bryan et al. 2014; last described in Brummel-Smith et al. 2019) using a flat Planck Collaboration et al. (2014) ΛCDM cosmology ($1 - \Omega_\Lambda = \Omega_\mathrm{m} = 0.285$, $\Omega_\mathrm{b} = 0.0461$, $h = 0.695$). We focus here on a single halo (named "Tempest") selected to ultimately have a Milky Way-like mass at $z = 0$ and no major mergers for $z < 1$. The selected halo has $R_{200} = 31\,\mathrm{kpc}$ and $M_{200} = 4 \times 10^{10}\ \mathrm{M}_\odot$ at $z = 3$, with dark matter particle mass $m_\mathrm{DM} = 1.39 \times 10^6\ \mathrm{M}_\odot$. This halo resides in a cosmological domain with a size of 100 comoving Mpc/h. The AMR is allowed to reach a maximum of 11 levels of refinement, corresponding to a finest spatial resolution of 274 comoving pc or a physical resolution of 68 pc at $z = 3$.

The simulations include metallicity-dependent cooling and a metagalactic UV background (Haardt & Madau 2012) using the Grackle chemistry and cooling library (Smith et al. 2017). Stars are formed in gas exceeding a comoving number density of $\simeq 0.1\,\mathrm{cm}^{-3}$ with a minimum star particle mass of $2 \times 10^4\,\mathrm{M}_\odot$. Following Cen & Ostriker (2006), supernova feedback is comprised of purely thermal energy that is deposited into the 27 nearest cells surrounding the star particle, after 12 gas dynamical times have elapsed since the star particle formed. The total energy imparted is $1.0 \times 10^5 m_* c^2$, the total mass ejected is 0.25 m_*, and the total metal mass ejected is

$$0.025 m_* (1 Z_*) + 0.25 Z_* \quad (1)$$

In this way, all metals are tracked as a single combined field; thus, particular elemental abundances throughout the paper are calculated assuming solar abundances and ion fractions are computed using the Trident package

(Hummels, Smith, & Silvia 2017). The effects of Type Ia SNe are not included.

The general aim of AMR simulations is to place refinement in areas that are the most physically interesting. Typically with these types of cosmological zoom-in simulations, the additional refinement is triggered primarily by increases in density, with the goal of best refining the dense, star-forming disk of the galaxy of interest. For each level of refinement, the cell size decreases by a factor of two such that

$$\text{Cell Size} = \frac{\text{Box Size}}{\text{Root Grid Cells}} \times 2^{-N_{\rm ref}}, \qquad (2)$$

where $N_{\rm ref}$ is the level of refinement; our root grid is 256^3. In our standard AMR simulations, the CGM typically reaches a refinement level of 6–8 while the ISM reaches $N_{\rm ref} = 11$. This corresponds to 2.2–0.55 kpc resolution in the CGM at $z = 3$. However, as discussed in Paper I, there are many processes relevant to circumgalactic physics acting on potentially smaller spatial scales, the cooling length being the most notable of these scales.

This first generation of FOGGIE simulations takes a different approach and targets cells for refinement based on their spatial location alone. This "forced refinement" scheme follows the targeted galaxy with a cubic box that tracks it through the domain. To implement forced refinement, we first run a "standard" AMR simulation as described above, writing out snapshots in 20 Myr increments. The main halo is identified and the coordinates of a 200 kpc comoving box centered on the galaxy are recorded for each snapshot. The simulation is then restarted at $z = 4$ with the volume enclosed by this box refined to a minimum refinement level; for our default $N_{\rm ref} = 10$ run (the "high-resolution" simulation in Paper I), this corresponds to a fixed resolution of 380 $\rm h^{-1}$ comoving parsec. We have additionally evolved an $N_{\rm ref} = 11$ simulation (190 $\rm h^{-1}$ comoving pc) to $z = 2.5$ with a cell size of 380 $\rm h^{-1}$ comoving pc ($N_{\rm ref} = 10$) or 190 $\rm h^{-1}$ comoving pc ($N_{\rm ref} = 11$). The location of the box is updated every 20 Myr. At $z = 3$, the two highly refined runs have physical spatial resolutions of 137 pc ($N_{\rm ref} = 10$) and 68 pc ($N_{\rm ref} = 11$) respectively. Throughout the rest of this paper, we will reference the normal AMR run as "standard" while the two highly refined runs will be referred to by this physical size of the refined CGM cells.

We emphasize here that nothing has changed between any of the runs presented throughout this paper *except the CGM resolution*. In particular, the ISM is simulated to the same resolution in all the runs as well as the star formation, feedback, and metal cooling prescriptions. That is, any physical processes arising in the higher resolution simulation, such as the ability of the gas to cool as the cooling length is resolved, are emergent phenomena rather than newly-implemented subgrid recipes. Any changes in the ISM are the result of changes in the CGM resolution affecting the flows of gas into and out of the ISM. The entire volume is shown in all plots so the effect on the ISM can be ascertained. In general, as most clearly seen in both the physical and surface brightness radial profiles (Figures 3 and 6), there is not much difference in the properties of the dense gas close to both the main halo and the satellite substructure.

2.2. *Calculating Emissivities*

For the densities and temperatures typical of the CGM, the gas cools primarily through collisional excitation followed by radiative decay, leading to a n^2 dependence of line emission. For a given line, the brightest emission will therefore come from gas with temperatures that correspond to the peak of that line's cooling curve. Bertone et al. (2013) shows examples of the cooling curves that dominate cooling of the diffuse universe.

To calculate the emissivity in each cell, the simulation is post-processed using the photoionization code CLOUDY (version 10.0; Ferland et al. 1998). For each cell, the emissivity is calculated using CLOUDY tables parameterized by hydrogen number density ($n_{\rm H}$), temperature (T), and redshift. The metal line emissivity is then scaled linearly by the metallicity of each cell, which captures the dependence on metallicity produced by the Cloudy modeling.

First, we constructed CLOUDY look-up tables of emissivity as a function of temperature ($10^3 < T < 10^8$K, $\Delta \log T = 0.1$) and hydrogen number density ($10^{-6} < n_{\rm H} < 10^2$ cm^{-3}, $\Delta \log n_{\rm H} = 0.5$), facilitated by CIALoop [1] (Smith et al. 2008). The calculation assumes solar metallicity and abundances. The grid is then linearly interpolated for every cell to the correct temperature and $n_{\rm H}$. Finally, CLOUDY also assumes that the gas is in ionization equilibrium, accounting for both photoionization and collisional ionization. For consistency with Corlies & Schiminovich (2016), we use the 2005 updated version of Haardt & Madau (2001) as our extragalactic ultraviolet background (EUVB) throughout. The EUVB can contribute to the heating and cooling of the gas in the simulation. Overall though, the heating will be dominated by physical processes such as SN feedback. As for the cooling, for $T > 10^4$ K, which is the case for all CGM gas considered, Cloudy modeling shows that the cooling function assumed in the simulation varies somewhat with the ionization frac-

[1] https://github.com/brittonsmith/cloudy_cooling_tools

tion at the low metallicities found in the CGM but is dominated by the overall metallicity. Thus, the emission results, particularly for the detectable emission, are roughly agnostic to the choice of EUVB (Corlies & Schiminovich 2016).

Throughout this paper, the effects of self-shielding are not included in any of our calculations. At the time the simulations were run, the Grackle library did not include self-shielding, but a subsequent update (Emerick et al. 2019) has enabled all later generations of FOGGIE to include self-shielding (Zheng et al. 2020) . For these runs, gas referred to as dense in the CGM only rarely has a hydrogen density above $\sim$0.01 cm^3 and so is generally unaffected (Faucher-Giguère et al. 2010). However, for the denser ISM of the main halo and satellite galaxies, this lack of self-shielding means that the exact numerical predictions for the dense gas residing in the ISM are unreliable but the general trend of this gas emitting the most brightly remains true.

Similarly, the conditions of the ISM also mean that the cooling time is not resolved for many cells in this region. This issue would not be solved by including self-shielding. However, because of the high resolution in the CGM, we do in fact resolve the cooling time for the large majority of cells outside of the disk in our more highly resolved simulations. Thus, the predictions for the CGM which are the focus of this paper are reliable while the exact values for the ISM are not, although we expect the trends to remain the same.

3. PREDICTED EMISSION PROPERTIES

In this section we make predictions for the distribution of metal-line emission at $z = 3$ and demonstrate the role CGM resolution plays on the probability of its detection. We present surface brightness maps for Hα, Si IV, C III, C IV, and O VI in Section 3.1, radial profiles and covering fractions in Section 3.2, and the kinematic properties in Section 3.3.

3.1. *Surface Brightness Maps*

Figure 1 shows surface brightness (SB) maps of the entire $200h^{-1}$ comoving kpc high refinement region at $z = 3$ for our standard AMR simulation (left), the 137 pc simulation (middle), and the 68 pc simulation (right) for Hα and a number of metal lines. Because the standard run has varying cell sizes due to the AMR, we choose to force the pixel size to match the 137 pc simulation for easy comparison. The two highly refined simulations have pixel sizes matching their stated CGM resolution. The SB dimming of an object at this redshift is accounted for in all images throughout the paper. This colormap will be used throughout the paper and corresponds roughly to the probability of detection with current and upcoming instrumentation. Green corresponds to pixels that should always be detected ($\log_{10}$(SB) ≥ 3 photons s^{-1} cm^{-2} sr^{-1}), blue to pixels that will probably be detected ($2 \leq \log_{10}$(SB) < 3 photons s^{-1} cm^{-2} sr^{-1}), and pink to pixels that are formally possible to detect but push the limits of all instruments ($1 \leq \log_{10}$(SB) < 2 photons s^{-1} cm^{-2} sr^{-1}). Gray are pixels that will not be detected in the near future ($\log_{10}$(SB) < 1 photons s^{-1} cm^{-2} sr^{-1}). Detailed matches to two current instruments, KCWI and MUSE, are discussed in Section 5.

Table 1 gives the total luminosity of each line in the $200h^{-1}$ kpc comoving refinement region for each of the simulations. While the distribution of the observable emission is not greatly affected by the resolution, the total luminosity emitted in each line does change substantially with resolution. Hα changes by a factor of two from the standard simulation to the 137 pc simulation and C III and C IV change by over an order of magnitude. The changing distribution of density, temperatures, and metallicities in the gas are likely causing these discrepancies. The complex interplay of these properties and the shape of the cooling curves of each line make it hard to predict how resolution will affect the overall luminosity. While differences in the galactic disk may drive these luminosity changes, we reiterate that nothing about the physics or resolution of the ISM has changed between these simulations. Differences in the ISM can not be separated from the effect of better resolving the CGM and the corresponding inflows and outflows of gas from the galaxy.

The luminosities from the 68 pc simulation are closer to the 137 pc simulation for a number of emission lines (Hα, C IV) but still about an order of magnitude different for the others. As we discuss in detail in Section 4.1, the changing distribution of density, temperatures, and metallicities in the gas are likely causing these divergences. The complex interplay of these properties and the shape of the cooling curves of each line make it hard to predict how resolution will affect the overall luminosity.

In general, the regions of brightest emission remain centered on the galactic disk, where the exact numerical values are subject to larger uncertainties in the modeling as discussed in Section 2.2. Additionally, the stars extend as far as a few kpc from the center of the galaxy like the ISM and can be expected to dominate any light that could be detected. However, beyond a few kpc, the CGM is the dominant source of emission.

For the CGM, lines whose cooling curves peak at slightly lower temperatures, like C III, tend to be the

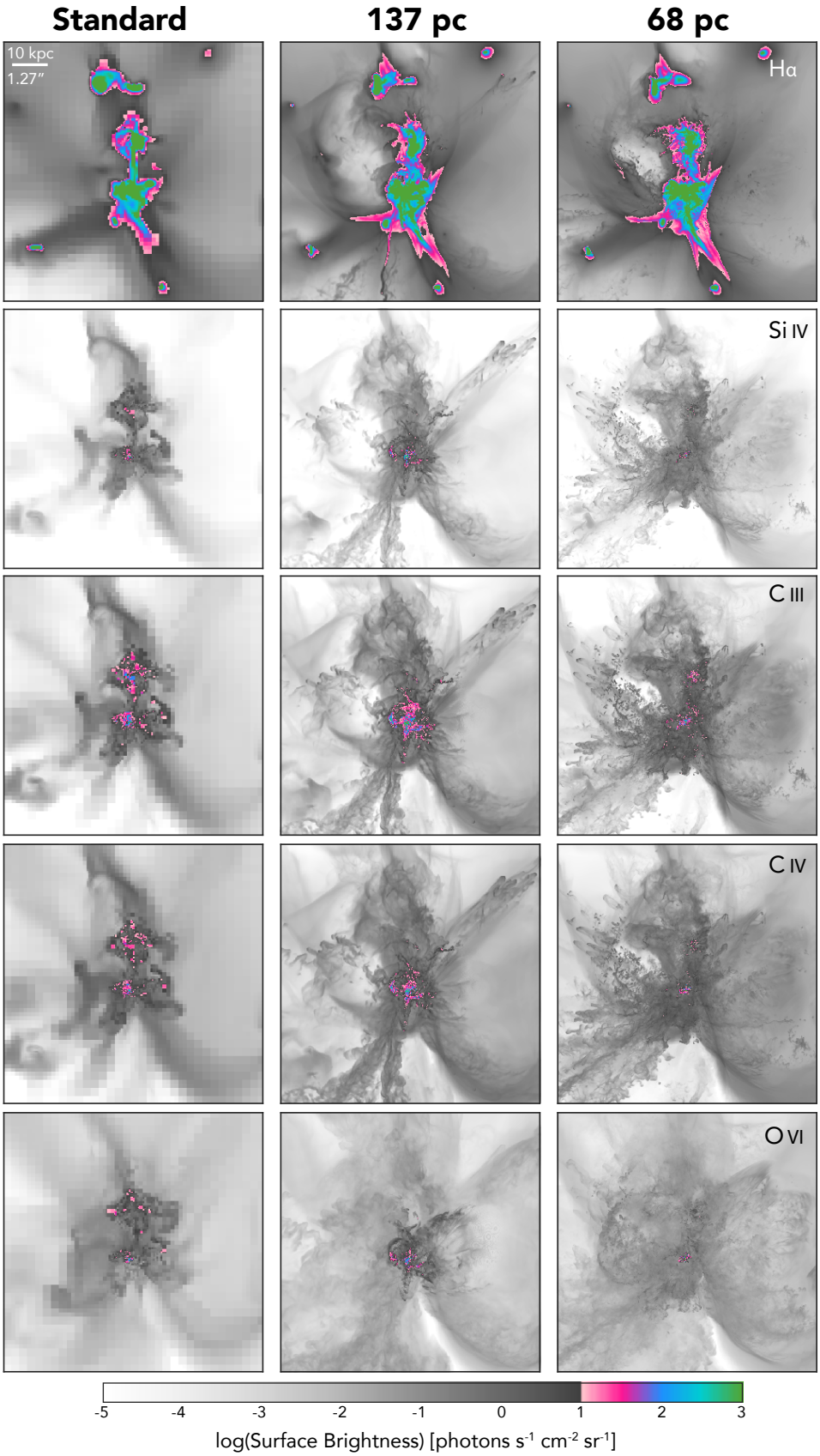

Figure 1. Surface brightness maps at $z = 3$ of five different emission lines (Hα, Si IV, C III, C IV, and O VI) for the standard AMR simulation, the 137 pc simulation, and the 68 pc simulation. The colors correspond roughly to detection probability with gray being non-detectable and colors related to different levels of likelihood as described in Section 3.1. The pixel size of the standard simulation is 137 pc and matches the CGM resolution in the two highly refined cases. Denser structures are clearly visible in the more highly refined simulations but most structures will remain beyond the detection limits of current and upcoming instrumentation.

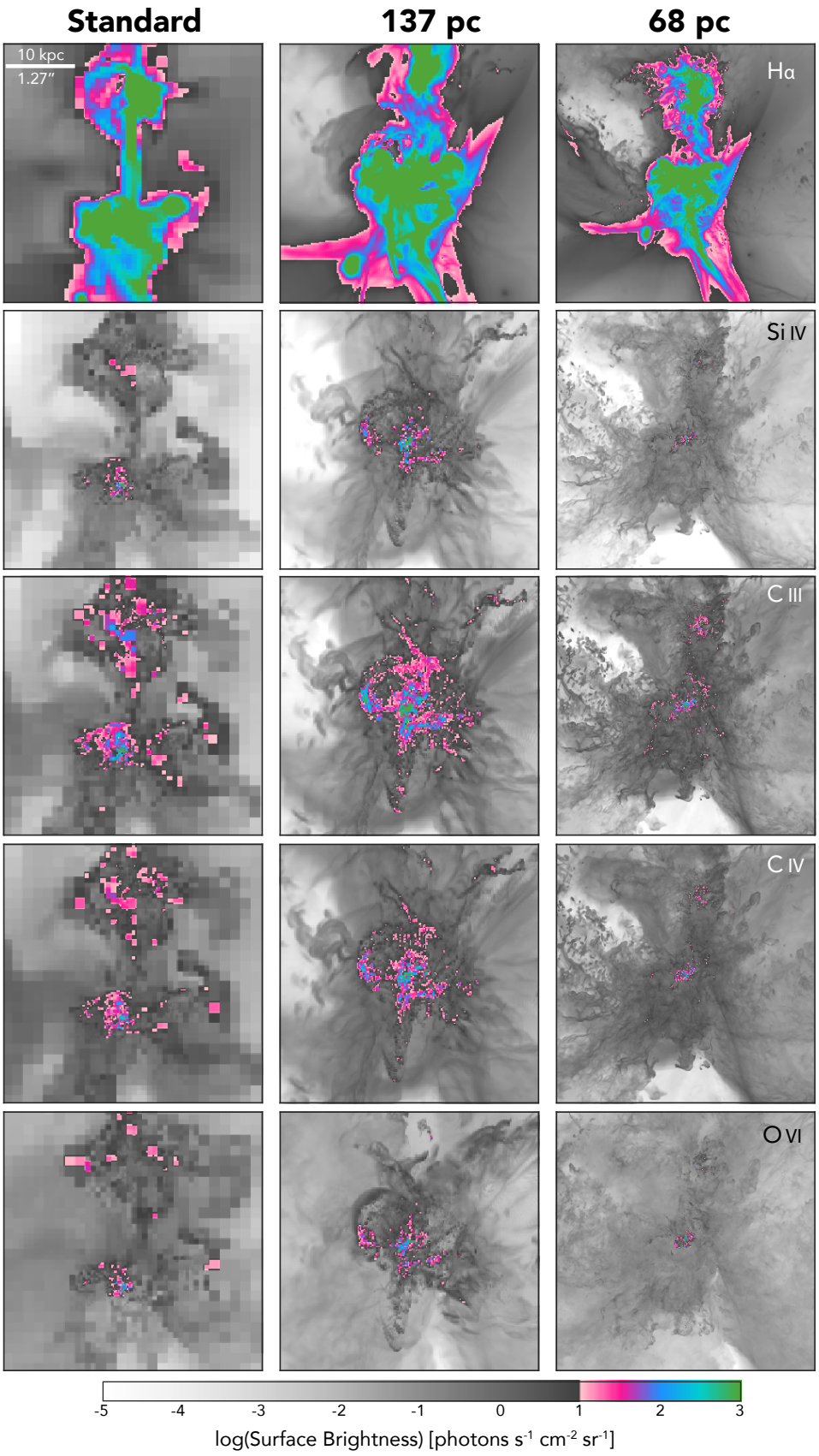

Figure 2. Same $z = 3$ surface brightness maps as Figure 1 but now zoomed in so only an area of 40×40 kpc ($5'' \times 5''$) is shown. The bright, observable emission is confined to within roughly 20 kpc of the galaxy. More disjointed areas can have higher surface brightnesses in the higher resolution simulations where regions are allowed to collapse to higher densities.

Line	Wavelength	Standard	137 pc	68 pc
Hα	6563 Å	8.9e42	1.3e43	1.2e43
Si IV	1394 Å	1.6e40	4.7e41	7.2e42
C III	977 Å	1.2e41	3.5e42	4.5e43
C IV	1548 Å	8.1e39	5.6e41	3.2e41
O VI	1032 Å	5.5e39	1.4e40	2.1e41

Table 1. Total luminosity of a given line within the refinement box for each simulation in units of ergs s^{-1}. The standard simulation under predicts the luminosity in each line by roughly an order of magnitude compared to the highly refined simulations.

brightest at this redshift because it is at these temperatures where the bulk of the dense gas throughout the halo is found. O VI, on the other hand, is particularly weak because there is little dense gas at higher temperatures, resulting in little detectable emission. We address the physical causes of the emission further in Section 4.

Adding resolution to the CGM clearly reveals the filaments feeding the galaxy and the structure within them that is artificially smoothed by the poor resolution in the standard run (left panels). Other small-scale structure is created by SN-driven outflows and by gas stripped from inflowing satellites. If we want to examine the small scale structure in emission, these highly refined simulations are needed.

However, despite these significant morphological differences between the runs, most of this increased small-scale structure around this relatively small galaxy is undetectable, as exhibited by the color map. Almost all of the detectable gas remains within 20 physical kpc, regardless of the CGM resolution.

The one large outlier is Hα. Because it is independent of metallicity, the line is extremely bright even at $z = 3$, tracing the cosmic filaments. However, at $z = 3$, Hα has shifted to an observed wavelength of 2.6μm, well outside the bandpasses of the ground-based IFUs discussed in this paper. This does fall at a wavelength observable by NIRSpec on the *James Webb Space Telescope*; more detailed *JWST* predictions will be the focus of future FOGGIE simulations.

To better highlight the detectable regions, Figure 2 shows a zoomed in view of the galaxy that is 40 physical kpc across (or 5″×5″ at $z = 3$). Much of the clearly observable emission is coming from the central part of the galaxy and thus the interstellar medium as opposed to the CGM. Because of limitations in modeling the ISM discussed in Section 2.2, specific numerical predictions for the interstellar medium are not entirely reliable but are accurate in their representation of more emission. Yet, it is also obvious that the higher circumgalactic spatial resolution leads to the formation of small, dense regions and clearer filamentary structure throughout the CGM although it is almost entirely undetectable.

Finally, we point out that the standard simulation displayed here has a satellite galaxy in close proximity, which is the source of the blue/green pixels in the images that are offset from the main halo. Because this halo was chosen to have no major mergers at $z < 1$, its merger history at higher redshifts is more active. Finding a snapshot where the halo is isolated simultaneously in all three runs of the halo is challenging. Instead, in this section and those that follow, all plots show the entire refined volume so that any effects of the galaxy interactions—shocks, tidal features, changes in kinematics—will be considered. However, no substantial variations are seen in the surface brightness profiles or the radial profiles of the gas physical properties.

3.2. *Surface Brightness Profiles and Covering Fractions*

The emission maps of Figures 1 and 2 show by eye the differences in the extent and scale of emission in the CGM and how it depends on the simulation resolution. In this section, we quantify these differences with a focus on the observational implications by looking at the radial profile and covering fractions of the surface brightness.

Figure 3 takes every pixel shown in the emission maps of Figure 1 and plots the radial profile of the surface brightness for four emission lines for the given projection axis. The colors here are generally matched to the colorbar of Figure 1. Radial profiles averaging over the three primary simulation axes tend not to show much variation so this single axis is illustrative (Corlies & Schiminovich 2016). The radial profiles confirm that easily detectable emission is confined to the central parts of the galaxy. This combines both the ISM whose modeling is less reliable and the stellar continuum which we expect to dominate the emitted light. However, beyond this region, the CGM once again becomes the primary source of emission. In the CGM, the potentially detectable (blue and pink) pixels can be found as far as 10-15 kpc from the center of the galaxy, although Si IV in all simulations and O VI in the highly refined simulations are found to extend less far. Thus, confirming emission is from the CGM and not the ISM will depend on the angular resolution of the observation. While most pixels remain undetectable, the radial profiles also highlight how the low resolution in the standard run does not fully sample such low surface brightness structures in the outer CGM. The bulk trends, however, remain consistent between both these simulations as well as those found previously (van de Voort & Schaye 2013).

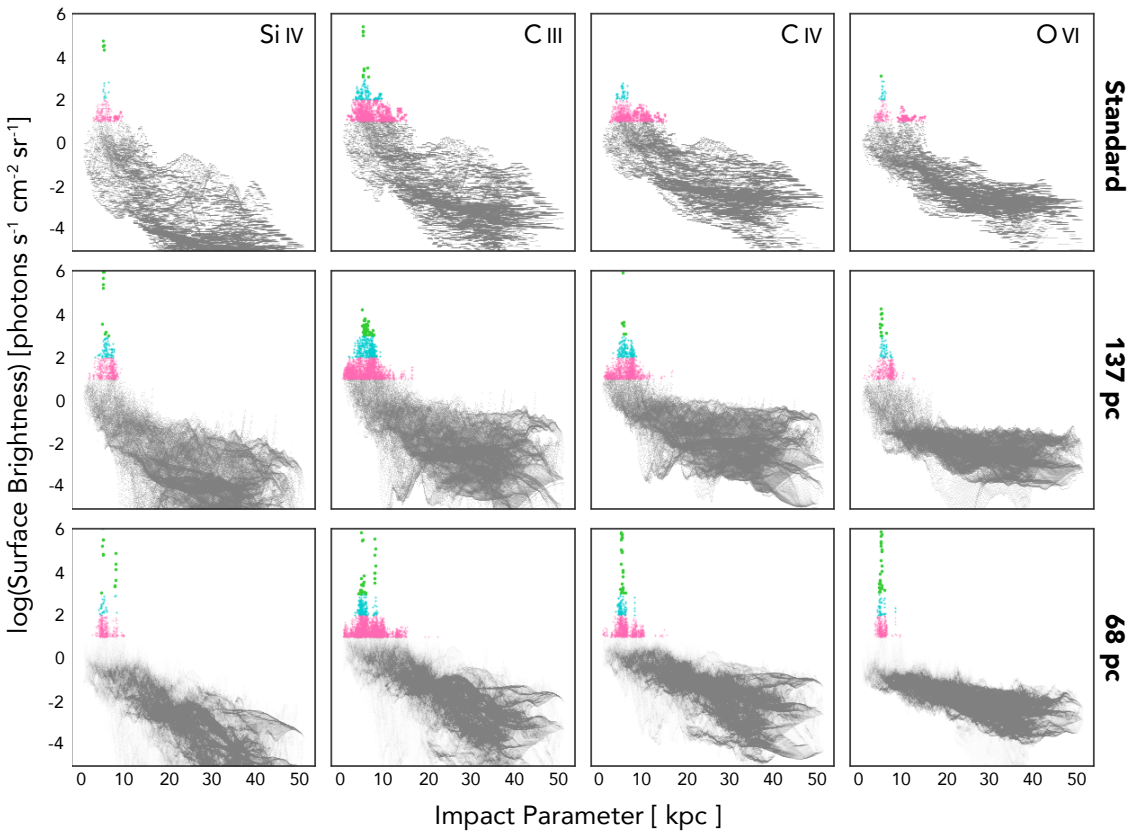

Figure 3. Radial profiles of the surface brightness maps shown in Figure 1 for four emission lines and all 3 simulations. The colors correspond to the color maps of Figures 1–2: green – detectable; blue/pink – possible to detect; gray – beyond current instruments. The detectable emission is found within 20 kpc for all the simulations. For non-detectable emission, structures within the CGM gas are much better traced in the simulations with better spatial resolution.

Figure 3's emission-focused radial profiles can be compared to the absorption-focused radial profiles in Figure 7 of Paper I. The emission seems to follow the H I column density the most closely with the brightest emission and the largest H I column densities being found within 20 kpc of the galaxy. However, the steepness of the SB profiles does not change as strongly with CGM resolution like it did for the column density profiles. This is in part because we have chosen to highlight the detectable emission so the plot spans almost 12 orders of magnitude on the y-axis. Looking instead at the undetectable pixels, more pixels exist at a larger spread of values so the radial profile is flatter for these larger radii. However, this similarity to the H I suggests that the main reason for these similar SB profiles is the strong dependence of the emissivity on the gas density whereas the number of pixels traces the volume-filling, diffuse gas.

Furthermore, observations of the SB profiles of galaxies similar to our own can provide a baseline check of the simulation predictions. From their sample of 26 galaxies at $3 < z < 6$, Wisotzki et al. (2016) found that the observed Lyα SB profiles had scale lengths of 4–5 kpc and extended as far as 10–20 kpc (see their Figure 7). These values are consistent with the extent of the potentially observable pixels for each simulated galaxy, indicating that the simulations provide reasonable results. The fact that these distances are detected in Lyα is reflective of the enhanced brightness of Lyα relative to the metal lines shown here.

We further quantify the observability of the emission by considering covering fractions of varying SB levels. Figure 4 shows the fraction of pixels above a given surface brightness level for four emission lines for each of the simulations. The covering fraction is then averaged over all three axes of the simulation box to reduce the influence of any preferential viewing angles.

In general, fewer than 1% of the pixels are detectable for any ion at the highest resolution of each simulation (and binned to 137 pc for the standard run). Above 10 photon s^{-1} cm^{-2} sr^{-1}, the 137 pc simulation does have a higher covering fraction than the standard simulation. The resolution affects the covering fraction in two ways. First, denser peaks are allowed to form

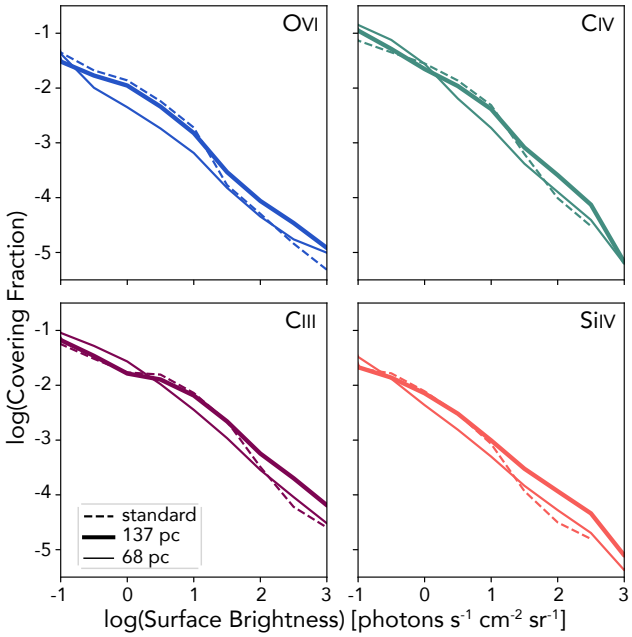

Figure 4. Number of pixels above a given surface brightness limit for four emission lines and all three simulations, averaged over the three primary projection axes of the simulation boxes. Fewer than 1% of pixels are observable and the fraction does not vary greatly with the simulation resolution.

because of the higher spatial resolution, which leads to brighter emission and more pixels above a given surface brightness limit in both of the highly resolved simulations. Second, the total number of pixels has gone up for both highly refined simulations. For the 137 pc simulations, allowing smaller, denser structures to exist has increased the bright pixels faster than the total number of pixels, increasing the covering fraction for a given surface brightness. On the other hand, for the 68 pc simulation, the overall number of cells increased faster than the number of bright cells found in smaller structures so the covering fraction has declined.

3.3. *Tracing Kinematic Properties*

A unique strength of using IFUs is that for every pixel, a spectrum is generated, providing kinematic information that can inform our understanding of the gas origins. To begin to estimate such properties from the simulation, we calculate the bulk velocity of the entire refinement region and subtract it from the cells within the box to provide a meaningful frame of reference for the gas velocities. Using this large of a volume captures the systemic velocity of the system more clearly than a velocity calculated using a small sphere centered on the halo to emphasize the rest frame of the stellar component because this galaxy is experiencing high rates of merging and accretion.

Figure 5 shows the emissivity-weighted line of sight (LOS) velocity at $z = 3$ for each simulation; the projection axis is the same as for the emission maps shown in Figure 1. We caution against directly comparing the simulations because the orientation of the galaxy relative to the projection axis is somewhat different in each simulation. Nevertheless, some general trends can still be identified.

Overall, the bulk movement and features of the velocity structure of the CGM agree on large scales between the simulations. Looking at each resolution individually, we see that in the standard simulation, there is not much variation in the velocity structure amongst the different emission lines. In contrast, in the highly refined simulations, while the bulk velocity flows remain similar, more small-scale velocity fluctuations are seen as the ionization energy of the line increases. Hα and the other low ions are tracing dense gas which is dominated by coherent filaments at these high redshifts. The higher ions, like O VI, trace the volume-filling gas which has more peculiar motions from outflows.

These maps demonstrate how the high resolution in the CGM changes the kinematics which in turn will affect the predicted emission line profiles, akin to the ways we showed how simulated velocity discretization affects absorption line profiles (Paper I). Thus, this resolution is crucial for using simulations to inform the interpretations of future observations of circumgalactic gas kinematics in emission.

4. CONNECTING EMISSION TO PHYSICAL CONDITIONS

Ultimately, the goal of observing the CGM in emission is to understand the physical properties—the density, temperature, metallicity, and ionization structure—of the gas. In this section, we explore how changes in emission properties can result from changes in the physical properties of the gas. These changes are solely due to improving CGM resolution, as no other parameters are varied.

4.1. *CGM Physical Properties and Resolution*

Figure 6 shows the radial profiles of temperature, hydrogen number density, metallicity, and a 1D-velocity for the three simulations presented throughout the paper. Here the center is taken to be the center of the refinement region, which is defined to track the main halo of interest. Because at this snapshot the halo is experiencing a merger, this center has shifted slightly to be closer to the center of mass of the merging system. The plots are mainly intended to investigate the distribution of the physical properties of the gas and the

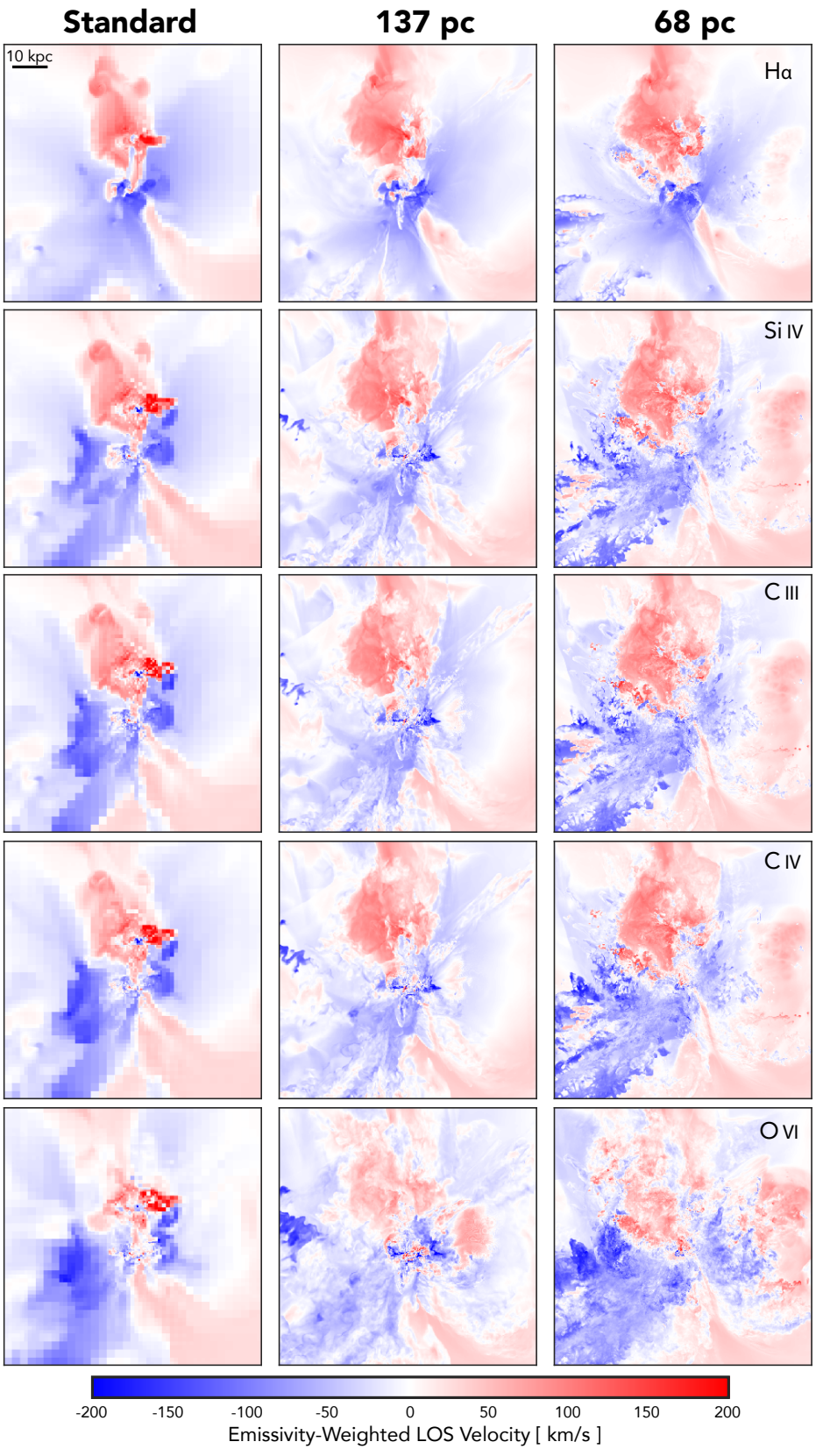

Figure 5. Maps of the emissivity-weighted LOS velocity after the bulk velocity of the refinement region has been subtracted. Direct comparisons between simulations is difficult because the orientation of the galaxy changes to match the emission maps shown in Figure 1. Overall, the bulk movement and features of the velocity structure of the CGM agree on large scales. Increasing the resolution increases variations in the kinematics amongst the different emission lines and reveals complex kinematic structures on the smallest scales.

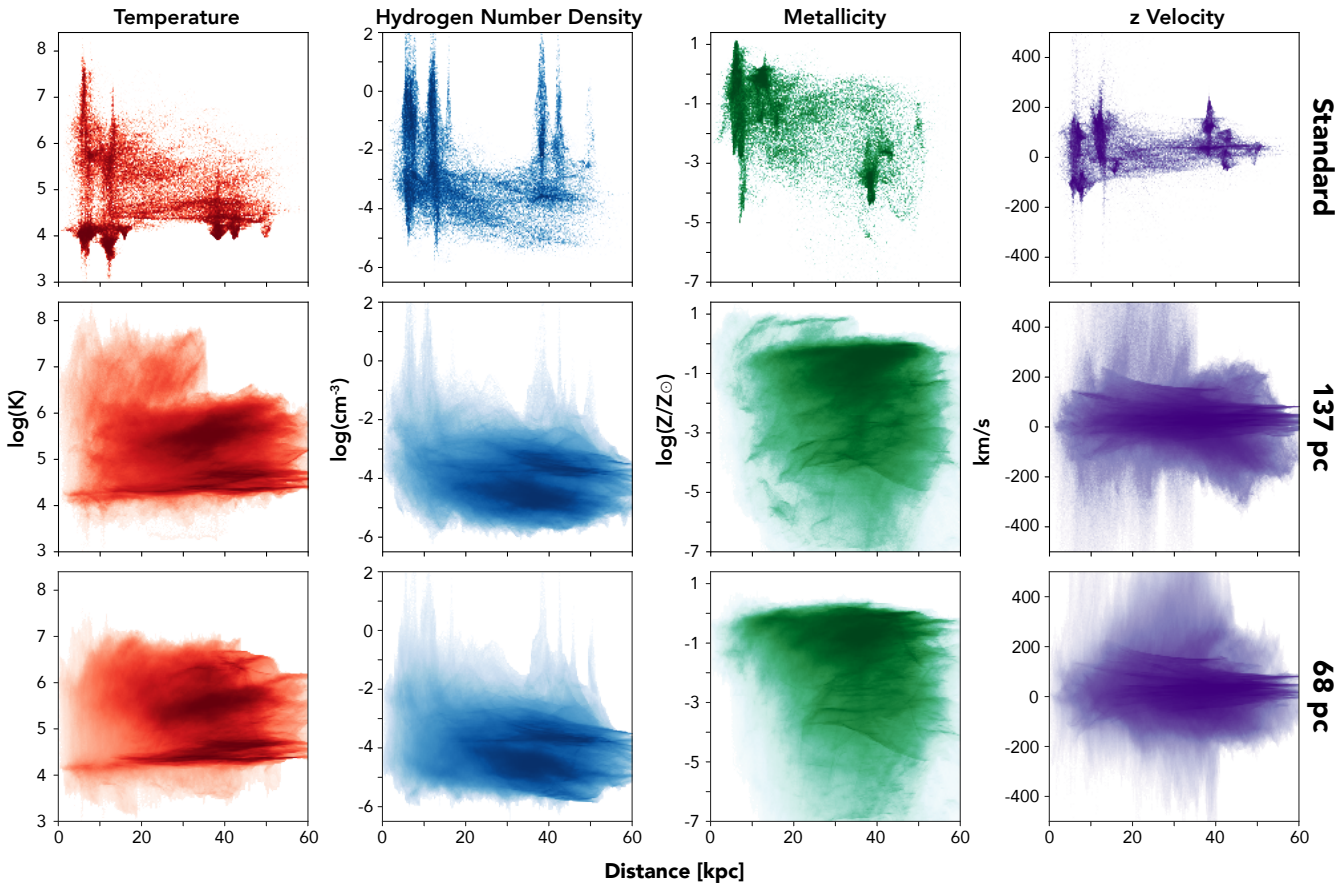

Figure 6. Radial profiles at $z = 3$ of the temperature, density, metallicity, and z-velocity for the three simulations discussed. Each cell in the volume is depicted such that fewer points corresponds to fewer number of cells in that simulation. While changing the resolution of the CGM does not affect the bulk, average properties of the gas, the spread in all of these physical quantities has changed dramatically at all radii.

main halo of interest is represented by the first peak in the density distribution for all simulations. The profile shows every cell within the simulation volume such that for the two highly refined simulations, it is displaying a volume-weighted radial profile. This was done intentionally to highlight the volume filling gas that the new refinement method is dedicated to resolving as well as to probe any structure within the volume. Weighting cells by mass instead does not change the trends in these distributions but just smooths away low-density structures that have formed in the gas.

In general, Figure 6 demonstrates that the *average* physical properties of the gas are unchanged, which is not surprising since all that varies between these simulations is the numerical resolution. However, we do see that the *breadth* of all of these quantities has increased. In the highly resolved CGM, gas can exist at low and high density, temperatures, metallicities, and velocities at all radii. That is, the gas is more multiphase at all radii in this halo at $z = 3$ when the CGM is more highly resolved.

A broader distribution of gas densities means there is more high density gas, which contributes to the higher total emission noted in Section 3.1 and shown in Table 1. Because the emission is predominantly produced by gas cooling through collisional excitation of these lines, the n^2 nature of this process means the strength of the emission depends strongly on density and can result in brighter emission. However, some of this dense gas might cool so far that emission from high ionization states are reduced while some gas may cool just enough to become denser but remain near the peak of the cooling curve of the ions presented here. This complex interplay of gas heating and cooling is why probing this gas in both emission and absorption is crucial.

Similarly, the small number of cells beyond the disk in the standard simulation means that the simulation can not sample the full range in temperature that the gas can exist in the CGM. When the emissivity of a cell is linked to the cooling curve, this means that some emission lines that emit where the temperature is poorly sampled (such as Si IV and C III for $10^{4.5} < T < 10^5$ K) will frequently be dimmer because more cells are falling in a higher temperature range, particularly for cells less than 25 kpc from the center of the galaxy (see the radial profiles of Figure 6). The increased resolution allows the gas to be more distributed in temperature, mitigating this problem. More gas can exist at the peak of the cooling curve of a larger number of metal lines.

Finally, the emissivity of the gas is also regulated by its metallicity. Just as the temperature changes when the gas is artificially mixed, so too does the metallicity. This helps explain why gas is not uniformly brighter in the high resolution simulations with denser gas. If the denser gas also now has lower metallicity, then the metal-line emission will not become as bright as gas at the same density but with higher metallicity from the artificial mixing.

In short, the combination of larger spreads in density, temperature, and metallicity result in more overall emission and in a different spatial distribution of such emission. The complicated interplay of these properties is why emission can be such a useful tool for diagnosing the CGM.

In the following subsections, we restrict our analysis to the standard and 137 pc simulations. Due to the sheer number of cells ($\sim 10^9$ in the forced refinement region) in the 68 pc simulation, detailed analysis of the outputs is difficult. Additionally, the differences between the two highly refined simulations are small compared to the differences between the standard and the 137 pc simulation. Providing a direct contrast between these two simulations makes the conclusions of the following sections clearer than including all three simulations.

4.2. *Examining the Ionization Process Driving Emission*

In addition to physical properties like density, temperature and metallicity, the source of the ionization of the gas is difficult to interpret from absorption spectra alone. Particularly, in the case of O VI, it is a long-standing debate if the O VI seen in absorption predominantly photo- or collisionally-ionized (Tripp et al. 2008; Savage et al. 2014; Werk et al. 2016; Oppenheimer et al. 2016; Nelson et al. 2018). Typically, the measurements are restricted to larger impact parameters where more quasars can be observed behind the foreground galaxies. The emission, on the other hand, is most observable for small radii close to the galaxy, providing a new way to explore this issue.

To investigate this question with our emission predictions, Figure 7 show the hydrogen number density ($n_{\rm H}$) and temperature weighted by the O VI emissivity along the line of sight for each pixel in the emission maps of Figure 1. In the top panels, the colors correspond to the average surface brightness of pixels that contribute to that bin, matching the color maps of Figures 1–3. The normalized histograms show the distribution of $n_{\rm H}$ and temperature for pixels falling within a given detectability bin. The phase diagrams show a clear trend that higher density leads to increasingly brighter emission. However, these dense regions also need to exist at the temperature at the peak of the cooling curve of that line to produce observable emission. Indeed, the observable

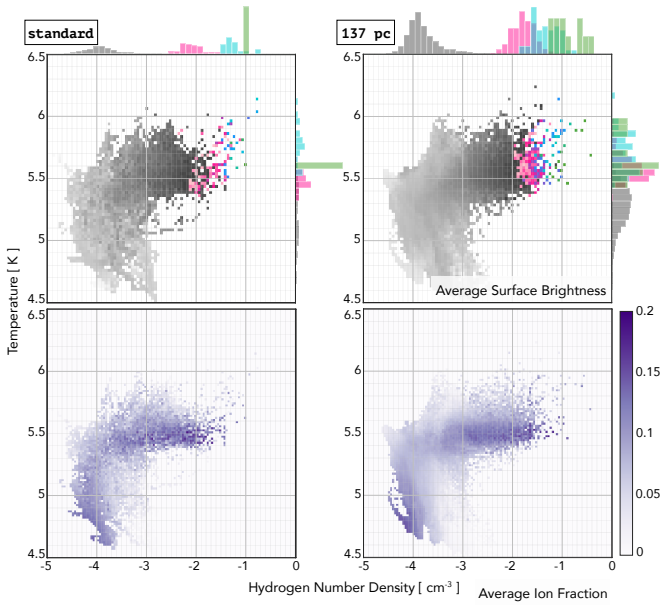

Figure 7. Hydrogen number density ($n_{\rm H}$) and temperature, weighted by the O VI emissivity. The left column shows the standard simulation and the right column the 137 pc simulation. In the top panels, colors correspond to the average surface brightness of pixels in each bin. In the bottom panels, colors show the average O VI ion fraction of pixels in each bin. The bottom panels show that high O VI ion fractions are generated by both photoionization (low density, low temperature) and collionsional ionization (high density, high temperatures). However, only the collisional ionization, which occurs near the peak of the O VI cooling curve, generates observable emission, as seen in the top panels.

bins all cluster around $T = 10^{5.5} - 10^{6}$ K for the O VI line.

Overall, there is not much variation between the two simulations in terms of the O VI-emitting gas. The phase space is clearly more finely sampled by the higher resolution run, and a slightly wider range of densities and temperatures contribute to detectable pixels, most likely because the metallicity has increased for some of the pixels.

The bottom panels show the same phase diagrams but colored to show the average ion fraction of pixels contributing to that bin. In both simulations, there is a large fraction of O VI for hot, dense gas (top right of each panel) representing collisionally ionized gas. There is also a peak in the O VI fraction at lower densities and at lower temperatures, revealing that there is also photoionzied O VI gas in the simulation. Thus, while both photoionized and collisionally ionized gas exists within the simulated CGM, only the collisionally ionized gas produces emission that is potentially bright enough to observe.

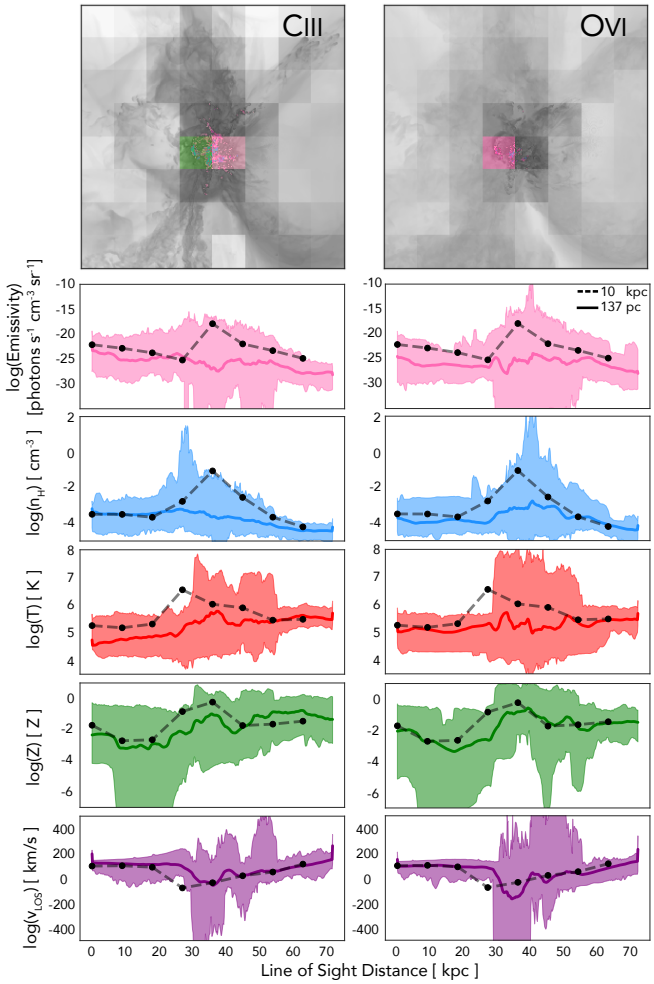

Figure 8. Top panels show the emission maps of C III and O VI for the 137 pc simulation at its fiducial resolution and for an overplotted image where the resolution has been degraded to 10 kpc. The pink pixel in both coarse images is found and the corresponding region in the high resolution image is identified. The LOS properties of the coarse simulation are then plotted in the lower panels as gray, dotted lines and of the highly refined simulation in solid colors. The solid colored line corresponds to the median values and the shaded region shows brackets the minimum and maximum value at each LOS position. The coarse resolution blends the gas physical properties such that the actual range of that gas's physical values is not sampled, limiting what can be inferred from such a measurement.

4.3. *The Effect of Angular Resolution on Deriving Physical Gas Properties*

Finally, the high resolution simulations can help place constraints on the degree to which the CGM properties are artificially blended by both coarse spatial resolution in the simulations and coarse angular resolution in the observations. The top panels of Figure 8 show the emission maps for two lines, C III and O VI, from the 137 pc

simulation and overplotted is the same image but where the pixel size is degraded to 10 kpc. The color map matches that of Figures 1–3. Visually, a single given observable pixel in the coarse image corresponds to a complex region with a large range of surface brightnesses and gas structures in the high resolution simulation. A single pixel whether simulated or observed is unable to capture such variations in CGM physical properties.

To understand this variation, we de-project the cube used to generate the emission map to recover the LOS information. We first identify the position where the pink pixel is found in the 10 kpc map and the corresponding region in the 137 pc image. In the lower panels of Figure 8, we plot the physical properties along the LOS for the single pixel in the coarse map as gray, dashed lines. The line-of-sight variation of the emissivity, hydrogen number density, temperature, metallicity, and LOS velocity in the low resolution cube are evident. For the set of pixels in the corresponding region of the full resolution cube, the colored lines show the median values of the physical properties along the LOS and the shaded regions correspond to the minimum and maximum values at each distance. The high resolution demonstrates that the coarser resolution in either simulations or observations blends the gas properties such that their variation is decreased. Gas is neither as hot or as cold, as dense or as diffuse, as metal-rich or metal-poor, as out-flowing or in-flowing in the coarse image as it is in the highly resolved image.

Furthermore, the emission in a given 10 kpc region is ultimately being driven by a handful of pixels that represent much smaller spatial scales. The brightest pixels can have emissivities of 10^{-15} to 10^{-10} photons s^{-1} cm^{-3} sr^{-1} as opposed to the median values of 10^{-25} photons s^{-1} cm^{-3} sr^{-1}. How the properties of these bright pixels vary with the LOS and how these properties compare to what would be derived from CLOUDY modeling of the measured emission on these scales will be the focus of future work.

5. INSTRUMENT-SPECIFIC EMISSION MAPS

In general, the observability of emission from the CGM is determined by an instrument's SB limit. However, the angular resolution of the instrument also determines our ability to interpret any emission that is detected, as was discussed in Section 4.3. In this section, we combine an investigation of both SB limits and angular resolution for two real instruments. Here we re-present the surface brightness maps at $z = 3$ of the 137 pc simulation to reproduce the properties of two ground-breaking optical integral field units: KCWI on Keck and MUSE on the VLT. Direct detection of circumgalactic emission is one of the primary science goals for both of these instruments. Both have multiple observing modes, but we focus here on those which have the most sensitive surface brightness limits combined with the best angular resolution. This is the "full-slice" mode on KCWI and the "narrow field" mode on MUSE, the details of which we summarize in Table 2.

	KCWI	MUSE
Mode Name	Full Slice	Narrow Field
FOV	$20'' \times 33''$	$7.5'' \times 7.5''$
Angular Resolution	$0.5''$	$0.025''$
Bandpass	3500–5600 Å	4650–9300 Å
Exposure Time	30h	27h
SB Limit	7×10^{-21}	1×10^{-19}

Table 2. Summary of details of observing modes modeled in Section 5 for KCWI and MUSE. Surface brightness limits are giving in ergs s^{-1}cm^{-2}arcsec^{-2}.

Figure 9 shows the emission maps for the ions of interest at $z = 3$ for both instruments. The relative sizes of the field of view (FOV) are depicted in the first two columns; the third shows a larger version of the MUSE images for clearer comparison with the KCWI images. All images reflect the stated angular resolution of the instruments' observing modes from their respective websites[2,3]. For MUSE, the surface brightness limit is taken from Wisotzki et al. (2018) who observed in the wide field mode. In the narrow field mode we discuss here, the limits should be similar for all but readnoise-limited cases. However, we use this value as a good rule of thumb for this exposure time. We focus on the narrow field mode since the small scales of the emission that are the focus of this work may raise the mean SB measured per spaxel as the emission is concentrated by the higher resolution of the instrument.

The left panels of Figure 9 show how the large FOV of KCWI in this mode (corresponding to 158×260 physical kpc at $z = 3$) allows the entire CGM be observed simultaneously. In this way, a single observation can capture the processes shaping the inner and outer CGM, whether that is cosmic filaments, minor mergers, or starburst-driven or AGN-driven outflows.

MUSE has a mode the enables a FOV twice the size of the KCWI mode presented above, but here we have chosen to highlight the predicted performance of the instrument when operating with full adaptive optics. The superb angular resolution in the narrow mode allows for the details of the small-scale gas structure to be probed.

[2] https://www2.keck.hawaii.edu/inst/kcwi/configurations.html
[3] https://www.eso.org/sci/facilities/develop/instruments/muse.html

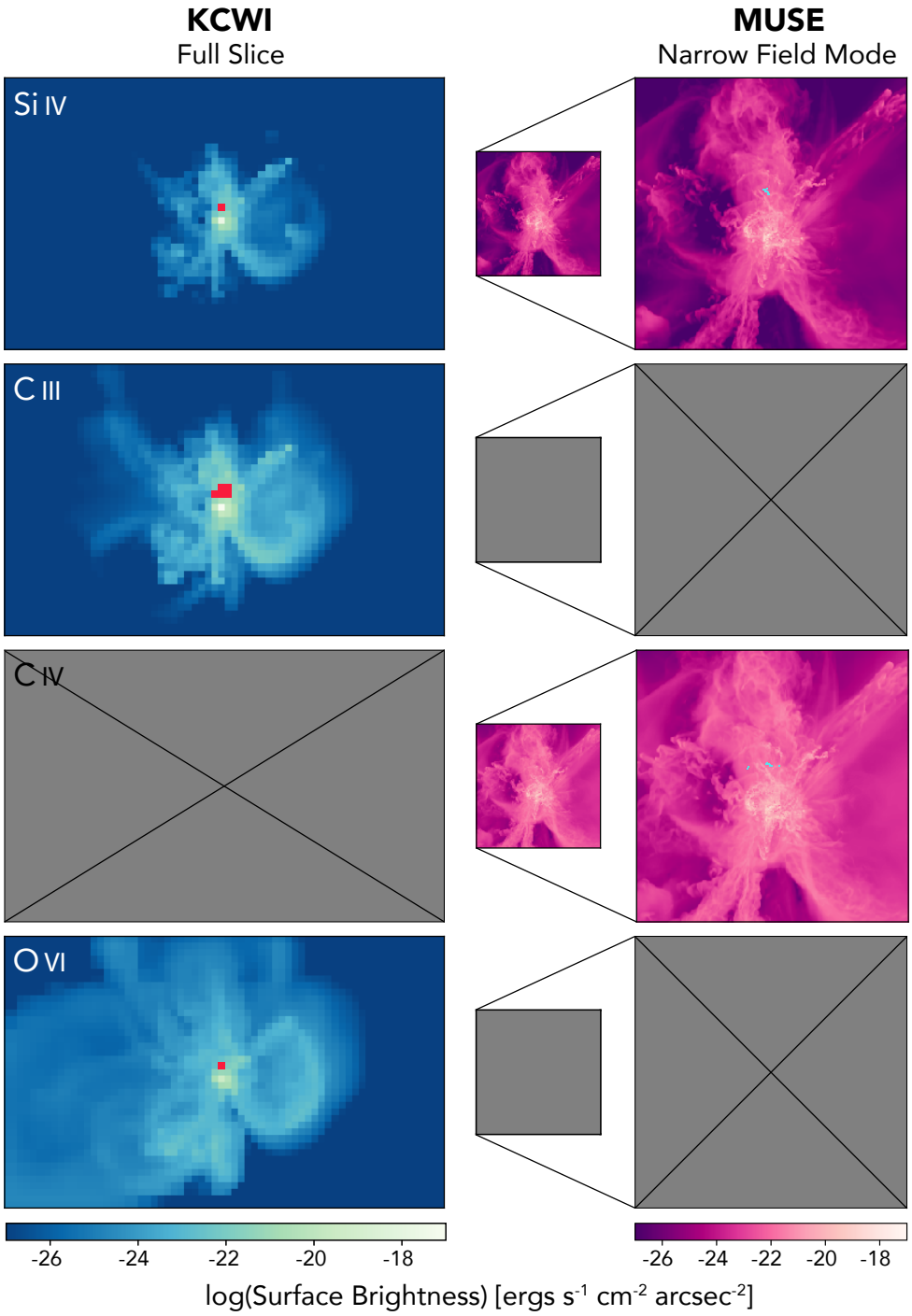

Figure 9. Emission maps to match the properties of two specific observing modes on KCWI and MUSE as outlined in Table 2. *Pixels that lie above the surface brightness limit of the instrument are colored to stand out from the colormap*: red for KCWI and blue for MUSE. Only a few pixels are detectable by either instrument. Gray boxes represent lines that have shifted out of the bandpass of the respective instrument and thus can not be observed at $z = 3$. The large FOV of KCWI allows the entire CGM to be observed simultaneously. MUSE has a similarly broad observing mode but here we highlight the "narrow field" mode, which has exceptional angular resolution. Such high angular resolution allows for a detailed look at the gas properties that are only resolved in the simulation because of our new refinement scheme.

The right panels of Figure 9 demonstrate how both high spatial resolution in the simulations and high angular resolution in the observations is needed to understand the distribution of physical and spatial properties of the CGM as laid out in the previous sections.

A major consideration that does not change with observing mode is the bandpass of the instruments. KCWI currently observes at much bluer wavelengths than MUSE. Because of the varying wavelengths of the emission lines, neither instrument can observe all of the metal lines presented here simultaneously. At lower redshifts, even more of the lines have shifted blue-ward of the MUSE bandpass. (Hα, which is detectable at $0 < z < 0.42$, is the notable exception.)

Despite the FOV, bandpass, and angular resolution trade offs, both instruments are ultimately limited by their surface brightness sensitivities. For the panes in Figure 9, pixels that are brighter than the limits of each instrument's observing mode are colored red for KCWI and blue for MUSE. For both instruments and for any line, there are at most a handful of pixels that clear the detection limit.

Binning (reducing angular resolution) or stacking (minimizing individual CGM features) may allow for better overall detection of the CGM emission. However, this single galaxy appears largely undetectable at $z = 3$ for these instruments. The goal of these predictions is to gain intuition for the detectability of CGM metal line emission around a Milky Way-like progenitor at high redshift. These calculations have not fully considered the PSF or optical systems of each telescope. This gas appears to remain mostly undetectable making such level of effort unnecessary. However, for future simulations targeting galaxies with brighter emission, accounting for these instrumental effects may provide value in guiding observations.

6. DISCUSSION

6.1. *Numerical Considerations of the New Refinement Scheme in Enzo*

The forced refinement algorithm that we use for these simulations has a different effect on the gas component of the simulation and the collisionless component (i.e., dark matter and star particles). When Enzo refines a grid cell, it subdivides the gas component into 8 equal volumes, and combines them when de-refining. In both the refinement and de-refinement processes, particles are left unsplit. In typical cosmological simulations refinement is approximately Lagrangian, and thus the number of particles per grid cell is kept at a roughly constant number (of order one to a few in dense regions). In the FOGGIE forced refinement simulations, however, this is not true—the number of grid cells exceeds the number of particles by a substantial margin. This can potentially be the source of issues, given Enzo's adaptive particle-mesh (APM) gravity solver, which deposits particles onto a grid using the cloud-in-cell algorithm, along with the gas density, in order to solve Poisson's equation. The CIC algorithm deposits a particle's mass into a volume $2\Delta x$ on a side, regardless of local spatial resolution or number of particles, meaning that the dark matter contribution can be highly localized in the forced refinement regions. One consequence of this discrete sampling is that it will introduce shot noise into the solution of the potential that may manifest as spurious heating of the gas from unphysical local potential gradients, and in principle may also act as a catalyst for the formation of multiphase gas (as dark matter particles may act as a local gravitational accretor. We argue that these phenomena are negligible. The velocity dispersion of the dark matter particles is comparable to the circular velocity of the halo, on the order of $100 - 200$ km/s. This is comparable to the typical sound speed in the halo ($\simeq 100$ km/s at 10^6 K), which suggests that a given particle's local interaction with a grid cell is comparable to the sound crossing timescale of that cell. It is, however, a much shorter time than the local cooling time (which is generally more than the sound-crossing timescale, except in cells that are thermally unstable). This means that the response of gas to discrete dark matter particles is typically going to be adiabatic, except in cells that are currently thermally unstable and in the process of isobarically collapsing to high relative density (and the likelihood of that occurring is low). This means that, while discreteness effects will likely impact the gas to some degree, it is likely to manifest as dispersed, spurious heating. We performed two further tests to estimate the impact of this numerical issue—one smoothing the dark matter particles over many grid cells at a given level, and a second that calculated the dark matter density only at coarse grid levels and then interpolated it to higher levels to calculate the potential rather than using CIC interpolation at those high levels. Neither test substantially affected the properties of the CGM, although they did substantially increase the computational cost of the calculations. As a result, we conclude that this particular numerical effect does not substantially impact our results.

6.2. *Observational considerations*

The instrument-specific emission maps shown above present a seemingly bleak picture for the future of directly detecting emission from the CGM. However, a more accurate statement is that they indicate that emis-

sion from *this* galaxy remains out of reach. While a Milky Way-like progenitor is interesting for understanding the evolution of galaxies like our own, this is not an ideal candidate to target for current emission observations. This galaxy has a total mass of only $4 \times 10^{10}\,M_\odot$, has a star formation rate of 3–4 $M_\odot\,yr^{-1}$, and has no active AGN. A more massive galaxy will likely have a denser CGM, be fed by stronger cosmic filaments, and have more in-falling satellites to provide dense, stripped material throughout its halo. Higher star formation rates and AGN feedback will eject more mass and metals into the CGM as well as generate more radiation to enhance photoionization and can lead to strong time variability in the emission (Sravan et al. 2016). This effect is seen at low-redshift in the COS-Bursts data low-redshift (Heckman et al. 2017) and at $z \sim 0.725$ by MUSE (Epinat et al. 2018). Thus, the prospects for more massive, active galaxies are promising for high-z studies.

In addition to looking at galaxies with more observationally favorable properties, this work also looks towards the development of extremely large telescopes (ELTs) that may search for the CGM emission of progenitors of Milky Way-like galaxies. With larger collecting areas, ELTs can push to even lower SB limits with the same angular resolution as current large telescopes, increasing our chances of detecting galaxies such as the one presented in this paper. However, there will be trade-offs: if the typical solid angle of the sky sampled by these new instruments is significantly smaller (e.g., to take advantage of the extreme adaptive optics corrections on the ELTs), the sensitivity to diffuse gas may remain little changed. Studies such as this one can help evaluate such trade offs in future instrument designs in light of different science goals.

Besides choosing galaxies with more favorable emission properties or lowering the surface brightness limit of observations, stacking remains a viable option for detecting emission from the CGM. While valuable information is lost pertaining to the exact gas distribution around each galaxy, stacking large numbers of galaxies shows that the extent of ionized gas is dependent on galaxy properties (Zhang et al. 2018a) and can be used to probe the dominant source of ionization of the gas at different galaxy masses (Zhang et al. 2018b). Large-scale cosmological simulations could also be used to mimic such a stacking procedure and examine any biases due to viewing angles and time variability though that is beyond the scope of this paper.

Furthermore, one of the biggest hindrances to detecting this emission is simply the distance and the resulting surface brightness dimming. Observing galaxies at lower redshift and in the UV, while still challenging, helps mitigate this particular limitation. Corlies & Schiminovich (2016) showed that emission from a Milky Way-like galaxy at $z = 0$ can potentially be detected as far as 120 kpc from the galaxy and that the covering fraction of detectable pixels can be as high as 5–10% depending on the surface brightness limit assumed. Similar fractions are predicted for a larger, cosmological volume by Bertone et al. (2010). UV-missions such as FIREBall-2 and LUVOIR may provide our most promising prospect for measuring the CGM in metal-line emission (Grange et al. 2016; The LUVOIR Team 2018).

Finally, this paper has focused on metal-line emission because of its usefulness it tracing large-scale galactic gas flows and probing the ionization state of the CGM. Despite the limitations in interpreting its emission, Lyman-α is expected to be at least times brighter than the next brightest emission line (Bertone et al. 2010). Future work will focus on combining these new, highly-refined simulations with a full radiative transfer code to make accurate predictions of Lyα emission maps and kinematics. Similarly, although Hα had the highest surface brightness, its long wavelength makes it unobservable by the optical IFUs we present here. However, this makes it a good candidate for observation with the *James Webb Space Telescope*; we will explore this potential in future work.

7. CONCLUSIONS AND FUTURE DIRECTIONS

Observing emission from the CGM would provide us with an unprecedented understanding of the 3D spatial and kinematic properties of how this gas is flowing into and out of galaxies, regulating their evolution. In this paper, we have focused on making metal-line emission predictions for the progenitor of a Milky Way-like galaxy at $z = 3$. Our novel approach to resolving the CGM has allowed us to probe structures on scales smaller than ever before and to understand how the physical properties of these scales link back to observable gas. All of the results we present here owe to changes in the simulated circumgalactic resolution alone, with no changes to the resolution of the interstellar medium or sub-grid physics recipes.

Our main conclusions are:

1. High spatial resolution in the CGM is necessary to better predict its emission properties. Improved spatial resolution allows gas to clump on scales smaller than resolved by typical cosmological simulations. These clumps form at large distances from the central galaxy but most remain undetectable in all of the simulations analyzed here, regardless of resolution.

2. Globally, increasing the CGM resolution alone appears to have a large effect on the total luminosity of the lines considered ranging from a factor of two (for Hα) up to two orders of magnitude (for C III and C IV).

3. Differences in the spatial distribution, covering fraction, and kinematic structures can be attributed to the broader range of physical properties the CGM possesses once it is more finely resolved.

4. Two instrument-specific maps for observing modes on KCWI and MUSE show that the emission from a small, low star-forming, high-redshift galaxy is generally not detectable. Simulations like these can be used to identify better candidates for direct detection in the future.

Moving forward, understanding the CGM will continue to be a science driver for future instrumentation, as it was for both KCWI and MUSE. Interpreting new IFU observations that probe small angular scales requires more simulations like the ones we present here that can achieve small spatial resolutions in the halo.

Future generations of FOGGIE simulations will include more massive galaxies as well as on those with more active merger and star formation histories. These systems will likely have a higher probability of detection of CGM emission from current instrumentation and provide a broader theoretical sample of highly-resolved galactic halos to guide target selection for future observations.

Observing galaxies at lower redshift will also improve the likelihood of detecting this gas by decreasing the amount of SB dimming. Thus, future FOGGIE simulations will also focus on expanding the size of our refinement region to encompass the entire virial radius of galaxies at $z = 0$ to make predictions for and inform the development of future UV observatories such as LUVOIR.

We gratefully acknowledge the National Science Foundation for support of this work via grant AST-1517908, which helped support the contributions of LC, BWO, NL, JOM, and JCH. LC was additionally supported in part by HST AR #15012. BWO was supported in part by NSF grants PHY-1430152, AST-1514700, OAC-1835213, by NASA grants NNX12AC98G, NNX15AP39G, and by HST AR #14315. NL was also supported by NASA ADAP grant NNX16AF52G. This work benefited from the successkid and sunglasses emoji on Slack. Computations described in this work were performed using the publicly-available Enzo code, which is the product of a collaborative effort of many independent scientists from numerous institutions around the world. Resources supporting this work were provided by the NASA High-End Computing (HEC) Program through the NASA Advanced Supercomputing (NAS) Division at Ames Research Center and were sponsored by NASA's Science Mission Directorate; we are grateful for the superb user-support provided by NAS. Resources were also provided by the Blue Waters sustained-petascale computing project, which is supported by the NSF (award number ACI 1238993 and ACI-1514580) and the state of Illinois. Blue Waters is a joint effort of the University of Illinois at Urbana-Champaign and its NCSA.

Facilities: NASA Pleiades, NCSA Blue Waters

Software: astropy (The Astropy Collaboration et al. 2018), CLOUDY (Ferland et al. 2013), Enzo (Bryan et al. 2014), grackle (Smith et al. 2017), yt (Turk et al. 2011)

REFERENCES

Arrigoni Battaia, F., Hennawi, J. F., Prochaska, J. X., et al. 2018a, ArXiv e-prints, arXiv:1808.10857

Arrigoni Battaia, F., Prochaska, J. X., Hennawi, J. F., et al. 2018b, MNRAS, 473, 3907

Augustin, R., Quiret, S., Milliard, B., et al. 2019, MNRAS, 489, 2417

Bacon, R., Accardo, M., Adjali, L., et al. 2010, in Proc. SPIE, Vol. 7735, Ground-based and Airborne Instrumentation for Astronomy III, 773508

Berg, M., Howk, J. C., Lehner, N., et al. 2018, in preparation

Bertone, S., Aguirre, A., & Schaye, J. 2013, MNRAS, 430, 3292

Bertone, S., & Schaye, J. 2012, MNRAS, 419, 780

Bertone, S., Schaye, J., Booth, C. M., et al. 2010, MNRAS, 408, 1120

Bordoloi, R., Tumlinson, J., Werk, J. K., et al. 2014, ApJ, 796, 136

Borisova, E., Cantalupo, S., Lilly, S. J., et al. 2016, ApJ, 831, 39

Borthakur, S., Heckman, T., Tumlinson, J., et al. 2016, ApJ, 833, 259

Brummel-Smith, C., Bryan, G., Butsky, I., et al. 2019, The Journal of Open Source Software, 4, 1636
Bryan, G. L., Norman, M. L., O'Shea, B. W., et al. 2014, ApJS, 211, 19
Butsky, I. S., & Quinn, T. R. 2018, ApJ, 868, 108
Cai, Z., Hamden, E., Matuszewski, M., et al. 2018, ApJL, 861, L3
Cen, R., & Ostriker, J. P. 2006, ApJ, 650, 560
Corlies, L., & Schiminovich, D. 2016, ApJ, 827, 148
Dijkstra, M., & Kramer, R. 2012, MNRAS, 424, 1672
Emerick, A., Bryan, G. L., & Mac Low, M.-M. 2019, MNRAS, 482, 1304
Epinat, B., Contini, T., Finley, H., et al. 2018, A&A, 609, A40
Faucher-Giguère, C.-A., Kereš, D., Dijkstra, M., Hernquist, L., & Zaldarriaga, M. 2010, ApJ, 725, 633
Ferland, G. J., Korista, K. T., Verner, D. A., et al. 1998, PASP, 110, 761
Ferland, G. J., Porter, R. L., van Hoof, P. A. M., et al. 2013, RMxAA, 49, 137
Ford, A. B., Werk, J. K., Davé, R., et al. 2016, MNRAS, 459, 1745
Frank, S., Rasera, Y., Vibert, D., et al. 2012, MNRAS, 420, 1731
Fumagalli, M., O'Meara, J. M., & Prochaska, J. X. 2016, MNRAS, 455, 4100
Grange, R., Milliard, B., Lemaitre, G., et al. 2016, in Proc. SPIE, Vol. 9905, Space Telescopes and Instrumentation 2016: Ultraviolet to Gamma Ray, 990531
Haardt, F., & Madau, P. 2001, in Clusters of Galaxies and the High Redshift Universe Observed in X-rays, ed. D. M. Neumann & J. T. V. Tran
Haardt, F., & Madau, P. 2012, ApJ, 746, 125
Hayes, M., Melinder, J., Östlin, G., et al. 2016, ApJ, 828, 49
Heckman, T., Borthakur, S., Wild, V., Schiminovich, D., & Bordoloi, R. 2017, ApJ, 846, 151
Hummels, C. B., Bryan, G. L., Smith, B. D., & Turk, M. J. 2013, MNRAS, 430, 1548
Hummels, C. B., Smith, B. D., & Silvia, D. W. 2017, ApJ, 847, 59
Hummels, C. B., Smith, B. D., Hopkins, P. F., et al. 2018, arXiv e-prints, arXiv:1811.12410
Keeney, B. A., Stocke, J. T., Pratt, C. T., et al. 2018, ApJS, 237, 11
Lake, E., Zheng, Z., Cen, R., et al. 2015, ApJ, 806, 46
Leclercq, F., Bacon, R., Wisotzki, L., et al. 2017, A&A, 608, A8
Lehner, N., O'Meara, J. M., Fox, A. J., et al. 2014, ApJ, 788, 119
Lehner, N., O'Meara, J. M., Howk, J. C., Prochaska, J. X., & Fumagalli, M. 2016, ApJ, 833, 283
Liang, C. J., & Chen, H.-W. 2014, MNRAS, 445, 2061
Martin, D. C., Chang, D., Matuszewski, M., et al. 2014, ApJ, 786, 106
Mitchell, P. D., Blaizot, J., Devriendt, J., et al. 2018, MNRAS, 474, 4279
Morrissey, P., Matuszewski, M., Martin, D. C., et al. 2018, ApJ, 864, 93
Neeleman, M., Wolfe, A. M., Prochaska, J. X., & Rafelski, M. 2013, ApJ, 769, 54
Nelson, D., Kauffmann, G., Pillepich, A., et al. 2018, MNRAS, 477, 450
Oppenheimer, B. D., Segers, M., Schaye, J., Richings, A. J., & Crain, R. A. 2018, MNRAS, 474, 4740
Oppenheimer, B. D., Crain, R. A., Schaye, J., et al. 2016, MNRAS, 460, 2157
Peeples, M. S., Corlies, L., Tumlinson, J., et al. 2019, ApJ, 873, 129
Péroux, C., Meiring, J. D., Kulkarni, V. P., et al. 2008, MNRAS, 386, 2209
Planck Collaboration, Ade, P. A. R., Aghanim, N., et al. 2014, A&A, 571, A16
Prescott, M. K. M., Momcheva, I., Brammer, G. B., Fynbo, J. P. U., & Møller, P. 2015, ApJ, 802, 32
Putman, M. E., Peek, J. E. G., & Joung, M. R. 2012, ARA&A, 50, 491
Quiret, S., Péroux, C., Zafar, T., et al. 2016, MNRAS, 458, 4074
Rafelski, M., Gardner, J. P., Fumagalli, M., et al. 2016, ApJ, 825, 87
Rhodin, N. H. P., Agertz, O., Christensen, L., Renaud, F., & Fynbo, J. P. U. 2019, MNRAS, 1416
Rosdahl, J., & Blaizot, J. 2012, MNRAS, 423, 344
Rubin, K. H. R., Prochaska, J. X., Koo, D. C., & Phillips, A. C. 2012, ApJL, 747, L26
Rudie, G. C., Steidel, C. C., Shapley, A. E., & Pettini, M. 2013, ApJ, 769, 146
Rudie, G. C., Steidel, C. C., Trainor, R. F., et al. 2012, ApJ, 750, 67
Salem, M., Bryan, G. L., & Corlies, L. 2016, MNRAS, 456, 582
Savage, B. D., Kim, T.-S., Wakker, B. P., et al. 2014, ApJS, 212, 8
Smith, B., Sigurdsson, S., & Abel, T. 2008, MNRAS, 385, 1443
Smith, B. D., Bryan, G. L., Glover, S. C. O., et al. 2017, MNRAS, 466, 2217
Som, D., Kulkarni, V. P., Meiring, J., et al. 2015, ApJ, 806, 25

Sravan, N., Faucher-Giguère, C.-A., van de Voort, F., et al. 2016, MNRAS, 463, 120

Stocke, J. T., Keeney, B. A., Danforth, C. W., et al. 2013, ApJ, 763, 148

Suresh, J., Nelson, D., Genel, S., Rubin, K., & Hernquist, L. 2018, ArXiv e-prints, arXiv:1811.01949

Suresh, J., Rubin, K. H. R., Kannan, R., et al. 2017, MNRAS, 465, 2966

Swinbank, A. M., Vernet, J. D. R., Smail, I., et al. 2015, MNRAS, 449, 1298

The Astropy Collaboration, Price-Whelan, A. M., Sipőcz, B. M., et al. 2018, ArXiv e-prints, arXiv:1801.02634

The LUVOIR Team. 2018, ArXiv e-prints, arXiv:1809.09668

Tripp, T. M., Sembach, K. R., Bowen, D. V., et al. 2008, ApJS, 177, 39

Tumlinson, J., Peeples, M. S., & Werk, J. K. 2017, ARA&A, 55, 389

Tumlinson, J., Thom, C., Werk, J. K., et al. 2013, ApJ, 777, 59

Turk, M. J., Smith, B. D., Oishi, J. S., et al. 2011, ApJS, 192, 9

Turner, M. L., Schaye, J., Crain, R. A., et al. 2017, MNRAS, 471, 690

Turner, M. L., Schaye, J., Steidel, C. C., Rudie, G. C., & Strom, A. L. 2014, MNRAS, 445, 794

—. 2015, MNRAS, 450, 2067

Tuttle, S. E., Schiminovich, D., Milliard, B., et al. 2008, in Proc. SPIE, Vol. 7014, Ground-based and Airborne Instrumentation for Astronomy II, 70141T

van de Voort, F., & Schaye, J. 2013, MNRAS, 430, 2688

van de Voort, F., Springel, V., Mandelker, N., van den Bosch, F. C., & Pakmor, R. 2019, MNRAS, 482, L85

Werk, J. K., Prochaska, J. X., Tumlinson, J., et al. 2014, ApJ, 792, 8

Werk, J. K., Prochaska, J. X., Cantalupo, S., et al. 2016, ArXiv e-prints, arXiv:1609.00012

Wisotzki, L., Bacon, R., Blaizot, J., et al. 2016, A&A, 587, A98

Wisotzki, L., Bacon, R., Brinchmann, J., et al. 2018, Nature, 562, 229

Wolfe, A. M., Gawiser, E., & Prochaska, J. X. 2005, ARA&A, 43, 861

Zhang, H., Zaritsky, D., & Behroozi, P. 2018a, ApJ, 861, 34

Zhang, H., Zaritsky, D., Werk, J., & Behroozi, P. 2018b, ApJL, 866, L4

Zheng, Y., Peeples, M. S., O'Shea, B. W., et al. 2020, arXiv e-prints, arXiv:2001.07736

Zheng, Y., Werk, J. K., Peek, J. E. G., & Putman, M. E. 2017, ApJ, 840, 65

Zheng, Z., Cen, R., Weinberg, D., Trac, H., & Miralda-Escudé, J. 2011, ApJ, 739, 62